Received: 28 May 2024 | Accepted: 29 July 2024

DOI: 10.1002/maco.202414491

ARTICLE

Materials and Corrosion

Hot corrosion behavior of Mo–Si–Ti alloys

Katharina Beck[1] | **Till König**[1] | **Ekin Senvardarli**[2] | **Frauke Hinrichs**[3] | **Martin Heilmaier**[3] | **Mathias C. Galetz**[1]

[1]High Temperature Materials, DECHEMA Research Institute, Frankfurt am Main, Germany

[2]Department of Materials Science and Engineering, Northwestern University, Evanston, Illinois, USA

[3]Institute for Applied Materials—Materials Science and Engineering, Karlsruhe Institute of Technology, Karlsruhe, Germany

Correspondence
Mathias C. Galetz, High Temperature Materials, DECHEMA Research Institute, Theodor-Heuss-Allee 25, 60486 Frankfurt am Main, Germany.
Email: mathias.galetz@dechema.de

Funding information
Deutsche Forschungsgemeinschaft (DFG), Grant/Award Number: 413956820

Abstract

The hot corrosion behavior of two ternary Mo–Si–Ti alloys (eutectic Mo–20.0Si–52.8Ti (at.%) and eutectoid Mo–21.0Si–34.0Ti (at.%)) was investigated at 700°C and 900°C for up to 100 h. Both Mo-based alloys evidenced a hot corrosion attack, resulting in a uniform attack of the substrate surface. The higher Ti content of the eutectic alloy significantly reduced the formation of solid and volatile Mo oxides compared with the eutectoid alloy. After 24 h at 700°C, the corrosion products formed on the eutectic alloy were only one-tenth the thickness of the layers formed on the eutectoid alloy. The corrosion products were examined with optical and electron microscopy. Semiquantitative electron probe micro analysis and X-ray diffraction measurements were used to identify the formed phases. The underlying corrosion mechanisms comprising not only hot corrosion-induced fluxing but also oxidation-induced pesting are discussed in detail.

KEYWORDS

high-temperature applications, hot corrosion, Mo-based alloys, silicides

1 | INTRODUCTION

As the gas temperatures of many high-temperature processes already exceed the maximum operating temperature of the commonly used Ni-based superalloys (1050°C[1]–1100°C[2]), air cooling of the hottest parts is required.[3] The incorporation of material systems with higher melting points could eliminate the need for external cooling and thereby significantly increase the efficiency of combustion processes. Beyond the required mechanical properties and oxidation behavior, the corrosive environment of combustion engines must also be considered for any new high-temperature material system.[4]

Hot corrosion is a common type of high-temperature corrosion occurring within turbines due to the formation of liquid salt deposits.[5–7] The main component leading to an increased attack is sodium sulfate.[8,9] During the operation of turbines, Na_2SO_4 is formed in situ from the reaction of NaCl (marine environments) in oxidizing atmospheres containing SO_2/SO_3 (sulfur-based impurities within the fuel and intake air).[10–12]

$$2NaCl(g) + SO_3(g) + \frac{1}{2}O_2 \rightleftharpoons Na_2SO_4(l) + Cl_2(g). \quad (1)$$

For Ni-based alloys two distinct types of hot corrosion have been established in the literature, which differ in temperature, salt composition, and the resulting damage characteristics.[12] The low-temperature type II hot corrosion occurs below the melting point of Na_2SO_4 in the

Abbreviations: EPMA, electron probe micro analysis; XRD, X-ray diffraction.

temperature range from 650°C to 800°C.[13,14] Reactions with substrate elements (Ni, Co) take place on the surface of the material and lead to eutectic compositions of sulfate salts with lower melting points,[15] which usually cause a localized pitting attack of the metal.[15,16] The high-temperature type I hot corrosion occurs between 850°C and 950°C and is caused by liquid Na_2SO_4 deposits.[16,17] This liquid breaches the protective oxide scale and continues to degrade the base alloy,[4] resulting in a uniform attack of the metallic material.[15]

Mo-based alloys, with their high melting points above 2000°C, are potential replacements for conventional Ni-based superalloys. Three-phase Mo–Si–B alloys have been intensely researched,[18,19] but some drawbacks like brittleness at room temperature and high susceptibility to pesting still remain. Significant progress was made through the development of metallic-intermetallic alloys in the Mo–Si–Ti system.[20] The eutectic alloy (Mo–20.0Si–52.8Ti (at.%)) consisting of a fine lamellar structure of bcc Mo_{ss} and hexagonal $(Ti, Mo)_5Si_3$ intermetallics demonstrates excellent oxidation resistance in the critical temperature range of 700–1300°C.[20–22] The eutectoid alloy (Mo–21.0Si–34.0Ti (at.%)) likewise exhibits a fine lamellar microstructure of bcc Mo_{ss} and tetragonal $(Mo, Ti)_5Si_3$ after the decomposition heat treatment at 1300°C but shows catastrophic oxidation in the temperature range of 700–900°C.[20–22] Nevertheless, both alloys had superior creep rates when compared with single crystalline CMSX-4 at temperatures above 1100°C.[20,23,24]

So far, the further development of this promising alloy system was focused on oxidation in air, with no information available to date about performance in more aggressive environments. A comprehensive understanding of hot corrosion behavior is available for Ni-based alloys, but potential refractory metal-based alternatives have received limited attention.[25–30] This study investigates the hot corrosion degradation of two ternary Mo–Si–Ti alloys (eutectic and eutectoid) under a Na_2SO_4 deposit in a SO_2/SO_3-rich gas at 700°C and 900°C.

2 | MATERIALS AND METHODS

2.1 | Alloying

The two ternary Mo–Si–Ti alloys (Mo–20.0Si–52.8Ti (at.%) and Mo–21.0Si–34.0Ti (at.%)) were prepared in an arc melter (Edmund Bühler GmbH AM/0.5) from the elemental materials (Mo, 99.95%, EVOCHEM; Si, 99.99%, ChemPUR; Ti, ⩾99.8%, ChemPUR). Before the arc melting process was performed at an Ar (>99.998%) base pressure of 600 mbar in a water-cooled Cu crucible, the vacuum chamber was evacuated to 10^{-4} mbar. To further reduce the residual oxygen in the vacuum chamber, a Zr getter was remelted before each melting step. The Mo–Si–Ti ingot was remelted five times and flipped after each step to ensure a homogeneous alloy. In a final drop casting step rods of 12–14 mm in diameter and a typical length of 150 mm were produced. After casting the eutectoid alloy was subjected to a heat treatment at 1300°C for 200 h under Ar (>99.998%) atmosphere in a resistance tube furnace (Carbolite Gero HTRH 70-600/18) to achieve eutectoid decomposition.

The resulting rods were arc wire cut to the required geometries (height of 3 mm and 12–14 mm in diameter) and ground with P500 silicon carbide paper to remove any Cu contamination possibly introduced by the wire erosion. Finally, the surfaces were cleaned in an ultrasonic bath with acetone.

2.2 | Hot corrosion

Na_2SO_4 (⩾99.0%, Alfa Aesar) coated samples (2.5 mg cm^{-2}) were exposed to the hot corrosion environment at 700°C and 900°C in the ranges of classical type I and II hot corrosion. Two different exposure times (24 and 100 h) enabled the investigation of the underlying attack mechanisms. The samples were placed in individual alumina crucibles inside a quartz tube furnace (Carbolite VST 12/900). The atmosphere of dry synthetic air (99.999%, Air Liquide) with 0.1% SO_2 (99.98%, Air Liquide) was passed through a Fe_2O_3 catalyst with a flow rate of 5 L h^{-1} before reaching the samples, enabling the oxidation of SO_2 into SO_3:

$$SO_2 + \tfrac{1}{2}O_2 \rightleftharpoons SO_3. \quad (2)$$

The p_{SO_3} of synthetic air + 0.1% SO_2 atmosphere at 700°C is around 5.3×10^{-4} atm and at 900°C approx. 1.3×10^{-4} atm, respectively.

The experimental setup was preheated at 150°C for 12 h under pure synthetic air to avoid the formation of sulfuric acid due to residual moisture before reaching the hot corrosion temperature with a rate of 10°C min^{-1}. Once the experiment was completed, the furnace was cooled down in synthetic air.

2.3 | Analytics

Macroscopic images were taken before and after the hot corrosion experiment with a Leica MZ16 A stereomicroscope. The scale formation was first investigated with X-ray diffraction (XRD) measurements using a Bruker D8 Advance A25 with Cu-K_α radiation. Then the samples were cold mounted in epoxy, halved, and

water-free ground with various SiC papers up to P2400 grit. Subsequently, the cross-sections were polished with 3 μm and 1 μm diamond suspensions and, as a final step, OPU relief polished to prepare them for microstructural analysis. Backscattered electron (BSE) images were taken with a Hitachi FlexSEM 1000II equipped with an energy-dispersive X-ray spectrometer (EDX). The oxide layer thicknesses were measured in at least four separate positions. These measurements were averaged, and the standard deviation was calculated. For further compositional analysis, a JEOL JXA-8100 electron probe microanalysis (EPMA) instrument equipped with five wavelength dispersive detectors (WDX) was used to obtain quantitative line scans and semi-quantitative element maps. The element distribution measurements were complemented by Raman spectroscopy (Renishaw inVia Raman Microscope) with a laser wavelength of 633 nm to analyze the phases formed by the corrosion products.

3 | RESULTS

3.1 | Eutectoid alloy (Mo–21.0Si–34.0Ti (at.%))

The surface zone of the eutectoid alloy corroded during exposure to a hot corrosion environment at 700°C and 900°C. BSE images and semiquantitative EPMA element maps of the cross-sections after 24 and 100 h of exposure are shown in Figure 1. At 700°C the oxide morphology looks very similar after both times, with the scale being thicker after the longer exposure time, resulting in further scale detachment (see Figure 1c). After both exposure times an inner oxide layer formed, comprised mainly of Mo oxides. The porous outer oxide layer is predominantly composed of TiO_2 and SiO_2, which also contains needle-shaped Mo oxide inclusions. The needle morphology of these inclusions is characteristic of MoO_3,[31,32] which was also identified via Raman measurements (see Figure A2).

At 900°C the eutectoid alloy was completely consumed after 100 h, while metallic substrate material could still be found under the thick oxide layer after 24 h. After both hot corrosion exposure times the inner oxide structure of the eutectoid alloy is similar to that formed after pure oxidation, a thick porous oxide layer comprised of TiO_2 and SiO_2.[20,22] The characteristic globular shape of the SiO_2 precipitates is in accordance with previous studies.[33] Compared with the samples that were exposed to 700°C, significantly fewer Mo oxides were found throughout the oxide layer. Instead, higher amounts of pores were present, which promoted scale detachment as the corrosion process advanced (see Figure 1c).

3.2 | Eutectic alloy (Mo–20.0Si–52.8Ti (at.%))

Figure 2 displays BSE images of the eutectic alloy along with the corresponding semiquantitative EPMA element maps to illustrate the progression of the hot corrosion attack. Compared with the eutectoid alloy, the oxide layers formed after both exposure times are significantly thinner. At 700°C after both exposure times a mixed TiO_2/SiO_2 layer formed, with the layer after 100 h being considerably thicker and exhibiting signs of scale spallation.

The hot corrosion temperature has a significant influence on the oxide morphology as evidenced by the formation of a duplex layer after the exposure at 900°C. EDX measurements, combined with XRD and EPMA data, revealed that there was an inner TiO_2-rich mixed oxide layer that incorporated small SiO_2 inclusions (see Figure 2e,g). This mixed oxide layer was in most parts covered by an outer, thinner SiO_2 scale, which contained small amounts of Na_2MoO_4. Interestingly, once established, the scale at 900°C did not change much between 24 and 100 h. At both temperatures, the corrosion front was free of MoO_3 and only smaller amounts of it were observed along with Na throughout the corrosion product without precipitates of MoO_3.

4 | DISCUSSION

4.1 | Eutectoid alloy (Mo–21.0Si–34.0Ti (at.%))

The eutectoid alloy was not able to form a continuous SiO_2 scale under hot corrosion conditions and high degradation rates were observed. Usually in this temperature range the thermally grown SiO_2 is amorphous,[34] while here, crystalline SiO_2 (cristobalite) was observed for all samples (see Figure A1). This is ascribed to the presence of the network modifier Na_2O, which has been reported to increase devitrification of SiO_2 in type I hot corrosion.[33] The hot corrosion environment preferentially attacked the solid solution phase Mo_{ss}, which is low in Si. The $(Mo, Ti)_5Si_3$ phase remains present in the oxide scale, where it is eventually oxidized. Due to this effect Mo-rich oxides and mixed Ti- and Si-rich oxides reflect the substrate microstructure in the inner corrosion scale at 700°C. Towards the gas/salt interface, the MoO_3 has volatilized, leaving behind a finely dispersed mixed oxide of SiO_2 and TiO_2, which is too porous to form a continuous protective layer. The selective attack of Mo_{ss}, the complete evaporation of MoO_3, and the unprotective Si and Ti oxide growth was observed for the eutectoid alloy in oxidation studies as

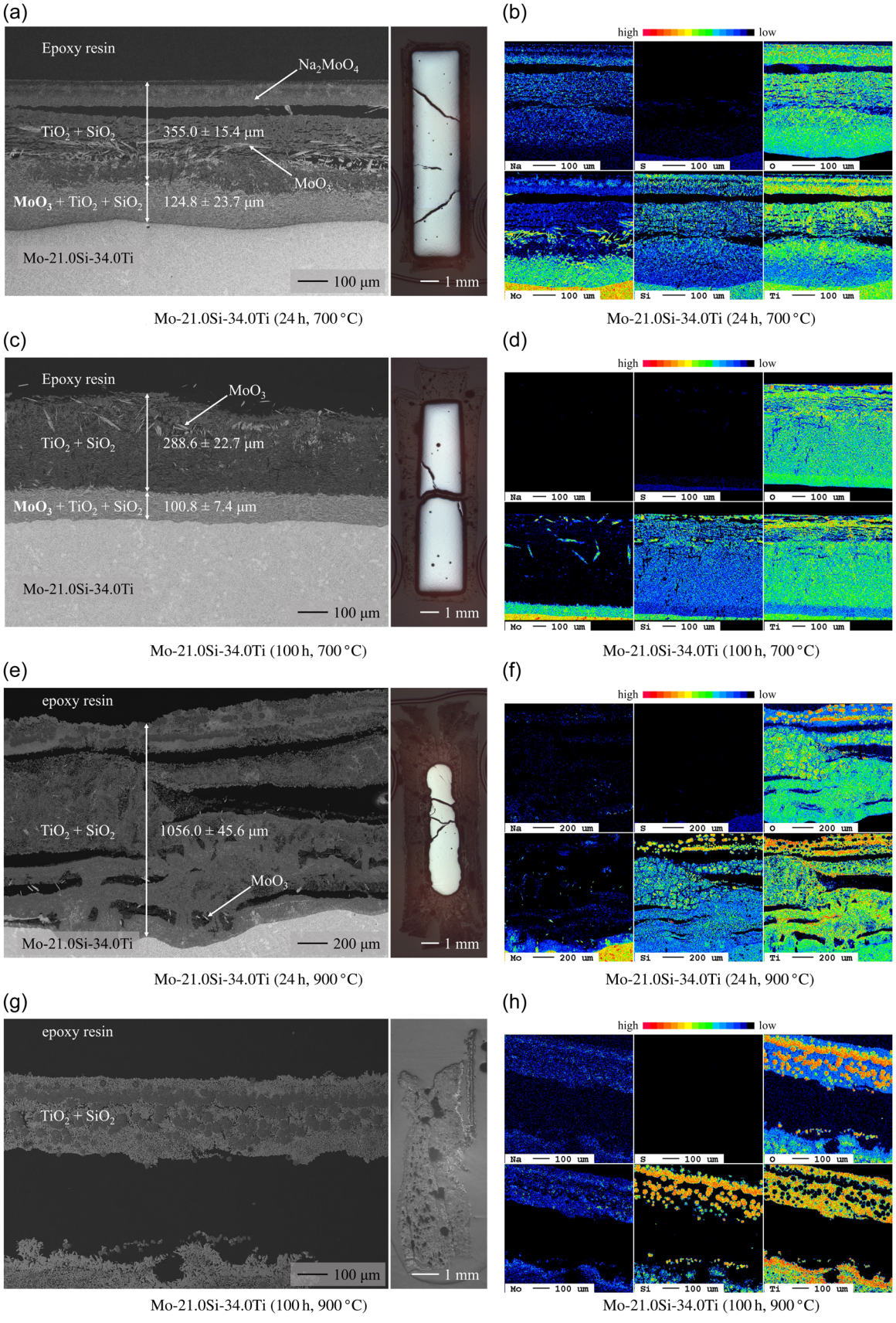

FIGURE 1 BSE images (a, c, e, g) and EPMA maps (b, d, f, h) of the oxides and corrosion products formed on the eutectoid alloy after hot corrosion in synthetic air + 0.1% SO_2 for 24 and 100 h. [Color figure can be viewed at wileyonlinelibrary.com]

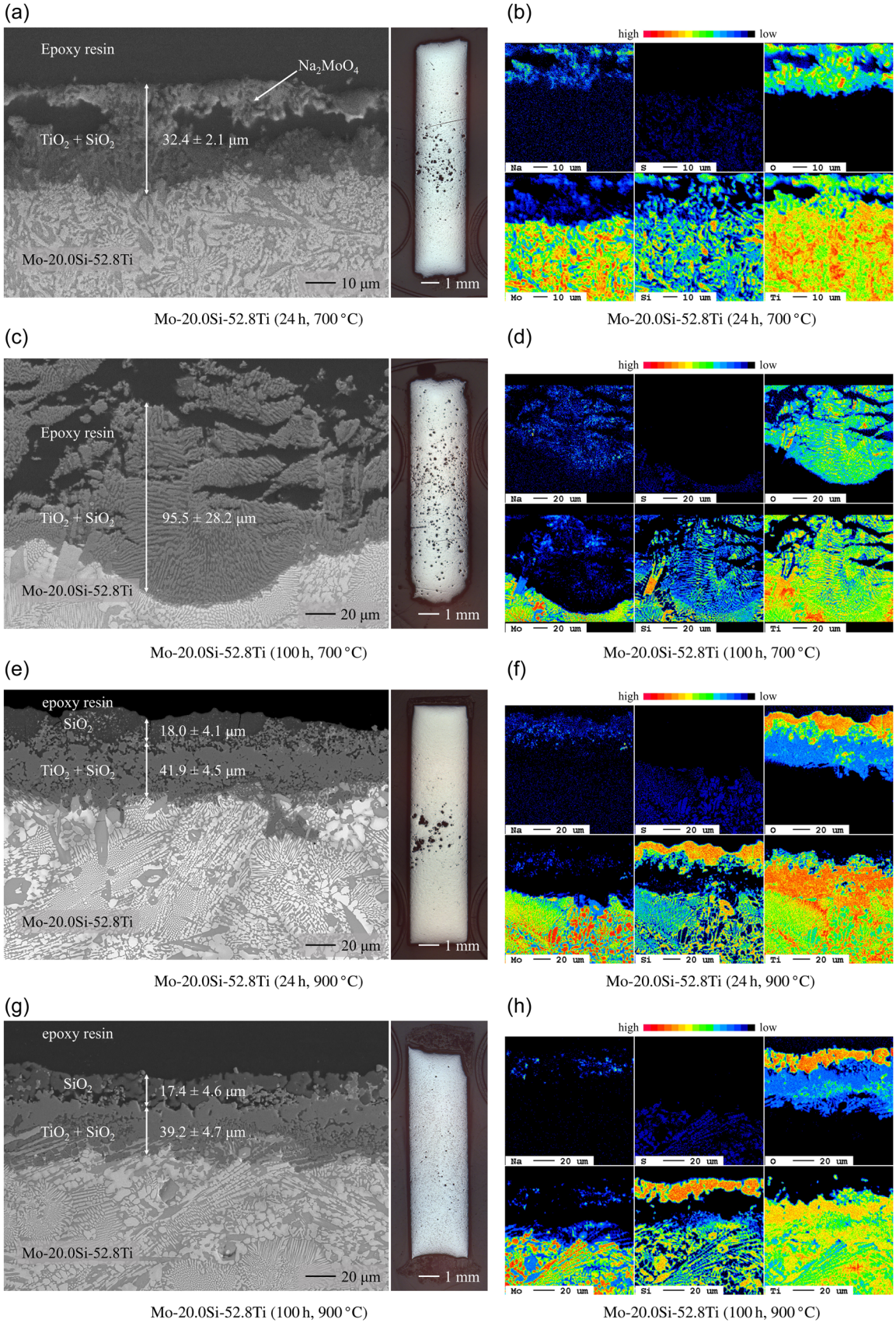

Mo-20.0Si-52.8Ti (24 h, 700 °C)

Mo-20.0Si-52.8Ti (24 h, 700 °C)

Mo-20.0Si-52.8Ti (100 h, 700 °C)

Mo-20.0Si-52.8Ti (100 h, 700 °C)

Mo-20.0Si-52.8Ti (24 h, 900 °C)

Mo-20.0Si-52.8Ti (24 h, 900 °C)

Mo-20.0Si-52.8Ti (100 h, 900 °C)

Mo-20.0Si-52.8Ti (100 h, 900 °C)

FIGURE 2 BSE images (a, c, e, g) and EPMA maps (b, d, f, h) of the oxides and corrosion products formed on the eutectic alloy after hot corrosion in synthetic air + 0.1% SO_2 for 24 and 100 h. [Color figure can be viewed at wileyonlinelibrary.com]

well,[20,22] which was attributed to pesting. Interestingly during hot corrosion of this alloy at 700°C, the evaporation of MoO_3 from the innermost corrosion product was prevented (likely by a molten salt as will be discussed subsequently), but still high degradation rates occurred. This is rationalized by the high oxygen diffusion in MoO_3,[35–37] which therefore did not significantly decrease the recession.

At 700°C, above the innermost layer was a section where MoO_3 was absent. Above this needles of MoO_3 were found, while the outermost corrosion product was again free of MoO_3. This microstructure is particularly well observable for MoO_3 in Figure 1a and schematically illustrated in Figure 3. The absence of MoO_3 in the outermost layer is expected, since MoO_3 undergoes pesting at the sample surface due to the high oxygen partial pressure.[38,39]

The needles of MoO_3 at 700°C (see Figure 1a,c) were not reported for pure oxidation and are presumably related to a supersaturation from a liquid eutectic, since their formation by solid-state diffusion appears unlikely. Their appearance can be explained by a dissolution and reprecipitation (fluxing) mechanism, which was discussed for the hot corrosion of Mo–9.0Si–8.0B (at.%).[30] The initially present Na_2SO_4 forms Na_2MoO_4 with MoO_3 according to the following equation:

$$MoO_3 + Na_2SO_4 \rightleftharpoons Na_2MoO_4 + SO_3. \quad (3)$$

Na_2MoO_4 is generally known for dissolving surrounding oxides,[40–42] and likewise, Na_2MoO_4 dissolves large amounts of MoO_3 in the present case. This results in the two eutectics 3 Na_2O–4 MoO_3 or Na_2O–4 MoO_3 with melting points down to 507°C and a MoO_3 content of more than 90% is needed for the formation of a solid phase at the test temperature.[43] Theoretically, for a continuous hot corrosion attack, the criterion of a negative solubility gradient must be met,[44,45] since otherwise, the dissolution would stop once the deposit is saturated with the dissolved species. In alloy-induced acidic fluxing, a saturation with MoO_3 is avoided, due to the evaporation of MoO_3 at the salt/gas interface. This is sufficient to explain a continuous degradation due to Na_2MoO_4 with the intermediate formation of MoO_3. As the evaporation occurs directly from the liquid phase, the formation of MoO_3 needles is not expected and can only be explained by decreasing solubility. This means the MoO_3 is dissolved in a region of high solubility (oxide/salt interface), whereas it precipitates in a region of low solubility (towards the salt/gas interface). The strongly acidic MoO_3 is expected to undergo basic dissolution, while it causes the surrounding oxides to undergo acidic dissolution. For hot corrosion, it is generally accepted that SO_3 strongly influences the salt acidity in contact with the gas phase. Considering Equation (3) as an equilibrium, it becomes clear that SO_3 can decrease the formation of Na_2MoO_4 and thermodynamic calculations indicate a suppression of this phase down to p_{SO_3} of ~10^{-5} atm (gas phase 5.3×10^{-4} atm).[46] Further, it decreases the Na_2O activity and thereby decreases the solubility of MoO_3, which fulfills the negative solubility criterion and gives a driving force for MoO_3 precipitation. This is a different mechanism compared with dry oxidation, but also results in a similar continuous degradation enhanced by Na_2MoO_4.

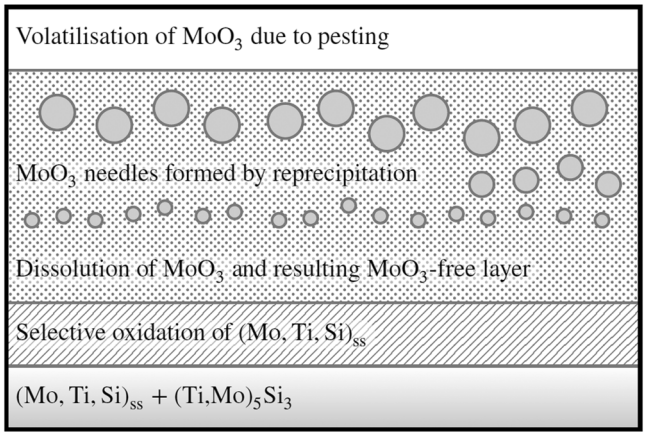

FIGURE 3 Schematic representation of the fluxing mechanism, which causes the reprecipitation of needle-shaped MoO_3 inclusions due to a negative solubility gradient in the salt melt.

At 900°C the evaporation of MoO_3 occurs directly upon precipitation from the liquid phase and the formation of MoO_3 needles is not observed, as the higher temperature leads to enhanced evaporation of these volatile compounds. However, after the depletion of MoO_3, Na_2MoO_4 remains present in the disintegrated sample, showing that this phase is less prone to evaporation. Just like the evaporation, the corrosion progress is much faster and after 100 h the sample is completely consumed.

4.2 | Eutectic alloy (Mo–20.0Si–52.8Ti (at.%))

For the eutectic alloy, MoO_3 is generally absent within the oxide layers after exposure at both temperatures. This is explained by the evaporation of MoO_3 as in the pesting mechanism, which prevailed during the corrosion attack and indicates a direct gas exchange to the corrosion front. A decreased corrosion rate along with the decreased Mo content favors the absence of MoO_3. But to stabilize solid

MoO_3 at the corrosion front, gas contact must be prevented, for example, by a molten deposit (eutectoid Mo–Si–Ti alloy) or low viscosity SiO_2 (as in Mo–Si–B alloys[30]). The formation of Na_2MoO_4 needs a decreased p_{SO_3}, which was apparently not established over the thinner and porous corrosion product. The formation of Na_2MoO_4 was only observed when encapsulated in SiO_2, as already reported for the Mo–Si–B alloy,[30] or below a thick corrosion product. Further, the amount of Mo available for Na_2MoO_4 formation is reduced and larger amounts of TiO_2 were formed.

At 700°C, the presence of the salt amplifies the attack in comparison to dry oxidation[22] by accelerating the degradation and thus preventing the formation of the outer mixed SiO_2/TiO_2 scale. At 900°C the salt seems to slow down the corrosion attack and an outer roughly 10 μm thick SiO_2 scale was observed. In type I conditions the dissolution of acidic oxides, like MoO_3, is known to increase the acidic solubility of other oxides. In this acidic regime, SiO_2 possesses only a low solubility, which is independent of the basicity.[47] The formation of a nearly closed SiO_2 top layer is therefore expected to be protective and the progress of the corrosion is minimal between 24 and 100 h. The formation of a pure SiO_2 top layer is a significant difference to the mixed TiO_2/SiO_2 layer observed for dry oxidation.[22] This SiO_2 top layer is also surprising, since O_2^- inward diffusion leads to oxide growth for SiO_2 layers[48] and during dry oxidation experiments mixed TiO_2/SiO_2 layers and TiO_2 top layers were found.[22] From a thermodynamic point of view, Si must oxidize readily in contact with the Mo oxides at the inner scale, due to the high stability of SiO_2. This challenges the assumption that SiO_2 cannot be dissolved in the molybdate.[47] Instead Na_2MoO_4 must play a critical role in the formation of the continuous several micrometer thick SiO_2 scale, which tremendously slows down the corrosion at 900°C. Considering the third alloying element Ti, the acidic dissolution of TiO_2 as Ti^{4+} ions is possible but was not conclusively demonstrated in the present case.

4.3 | Comparison of the Mo–Si–Ti alloys and Mo–Si–B

Consistent with previous oxidation experiments,[20,22] the hot corrosion behavior of the eutectic alloy is superior to that of the eutectoid alloy. During the hot corrosion of both alloys, the Mo_{ss} phase undergoes a more severe attack compared with the silicide phase. This preferential attack is known from the pesting literature and at 800°C a requirement for pesting resistance was a Ti-content of more than 35 at.% in the Mo_{ss}, which is achieved for the eutectic but not for the eutectoid alloy.[49] The increased overall Ti content and the resulting reduced Mo content also had a beneficial effect on the hot corrosion resistance (decreased recession rate compared with the eutectoid alloy) and resulted in the described change in microstructure. But in contrast to its pesting resistance at 800°C, the eutectic Mo–Si–Ti alloy was prone to hot corrosion at 700°C, due to the evaporation of MoO_3. Therefore, the Ti content in the Mo_{ss} is apparently insufficient to hinder this volatilization enough to form protective oxides.

In comparison to the well-researched reference Mo–9.0Si–8.0B (at.%),[30] the higher Si content of the investigated alloys was expected to improve hot corrosion resistance,[50–52] because of the low solubility of SiO_2 over a large range of basicity, which should decrease fluxing mechanisms.[27,47,53,54] The increased Si content did not lead to an improved hot corrosion behavior for the eutectoid alloy, since no continuous SiO_2 layer was established. In contrast, it is the decreased Mo content of the eutectic alloy which results in a lower degradation rate.

5 | CONCLUSION

To summarize, both Mo–Si–Ti alloys were subject to hot corrosion attack (700°C and 900°C, synthetic air + 0.1% SO_2, Na_2SO_4 deposit of 2.5 mg cm^{-2}), resulting in a uniform attack of the substrate surface. The mechanisms differed from the classical hot corrosion, and the severity of the attack and the corrosion products formed are highly dependent on the alloy composition. The eutectoid alloy experienced a combination of MoO_3 evaporation, dissolution, and reprecipitation (fluxing) as well as the selective oxidation of Mo_{ss}.

In contrast, the hot corrosion attack on the eutectic alloy was dominated by a pesting-like mechanism, even though the alloy has previously been proven to be pesting resistant in air. It was also observed that the silicide phase is significantly more resistant to hot corrosion than the Mo_{ss} phase. While still severely degraded, the eutectic alloy showed a significantly higher resistance to hot corrosion at 900°C, due to the formation of a nearly closed SiO_2 top layer.

AUTHOR CONTRIBUTIONS

Katharina Beck: Methodology; investigation; writing—original draft preparation; visualization. **Ekin Senvardarli**: Writing—Original draft preparation; visualization. **Till König**: Writing—review and editing; supervision. **Frauke Hinrichs**: Resources; writing—review and editing. **Martin Heilmaier**: Writing—review and editing; project administration; funding acquisition. **Mathias C. Galetz**:

Conceptualization; writing—review and editing; supervision; project administration; funding acquisition.

ACKNOWLEDGMENTS

The authors thank Dr. Gerald Schmidt for EPMA measurements, Mathias Röhrig for technical support and Susann Rudolphi as well as Daniela Hasenpflug for metallographic preparation. This work was supported by the Research Training Group 2561 "MatCom-ComMat: Materials Compounds from Composite Materials for Applications in Extreme Conditions" (project number: 413956820) funded by the Deutsche Forschungsgemeinschaft (DFG). Open Access funding enabled and organized by Projekt DEAL.

CONFLICT OF INTEREST STATEMENT

The authors declare no conflict of interest.

DATA AVAILABILITY STATEMENT

The data that support the findings of this study are available from the corresponding author upon reasonable request.

ORCID

Katharina Beck http://orcid.org/0000-0001-5751-6524
Till König http://orcid.org/0000-0001-8853-6608
Frauke Hinrichs http://orcid.org/0000-0001-8129-6648
Martin Heilmaier http://orcid.org/0000-0002-8983-4962
Mathias C. Galetz http://orcid.org/0000-0001-6847-2053

REFERENCES

[1] S. Walston, A. Cetel, R. MacKay, K. Ohara, D. Duhl, R. Dreshfield, in: *10th Int. Symp. Superalloys*. **2004**.
[2] A. Sato, H. Harada, A. C. Yeh, K. Kawagishi, T. Kobayashi, Y. Koizumi, T. Yokokawa, J. X. Zhang, *Superalloys* **2008**, *2008*, 131.
[3] J. H. Perepezko, *Science* **2009**, *326*, 1068.
[4] G. H. Meier, *Oxid. Met.* **2022**, *98*, 1.
[5] P. Kofstad, G. Åkesson, *Oxid. Met.* **1980**, *14*, 301.
[6] K. P. Lillerud, P. Kofstad, *Oxid. Met.* **1984**, *21*, 233.
[7] G. W. Goward, *J. Eng. Gas Turbine. Power* **1986**, *108*, 421.
[8] A. K. Misra, D. P. Whittle, W. L. Worrell, *J. Electrochem. Soc.* **1982**, *129*, 1840.
[9] F. Pettit, *Oxid. Met.* **2011**, *76*, 1.
[10] P. Hancock, *Corros. Sci.* **1982**, *22*, 51.
[11] V. Lemoine, P. Steinmetz, B. Roques, C. Duret, *Corros. Sci.* **1985**, *25*, 431.
[12] B. Grégoire, X. Montero, M. C. Galetz, G. Bonnet, F. Pedraza, *Corros. Sci.* **2018**, *141*, 211.
[13] J. Stringer, *Mater. Sci. Technol.* **1987**, *3*, 482.
[14] J. R. Nicholls, *JOM* **2000**, *52*, 28.
[15] R. Bürgel, H. J. Maier, T. Niendorf, *Handbuch Hochtemperatur-Werkstofftechnik: Grundlagen, Werkstoffbeanspruchungen, Hochtemperaturlegierungen und -beschichtungen*, Springer, Wiesbaden **2011**.
[16] N. Eliaz, G. Shemesh, R. M. Latanision, *Eng. Fail. Anal.* **2002**, *9*, 31.
[17] P. Hancock, *Mater. Sci. Technol.* **1987**, *3*, 536.
[18] D. M. Dimiduk, J. H. Perepezko, *MRS Bull.* **2003**, *28*, 639.
[19] J. A. Lemberg, R. O. Ritchie, *Adv. Mater.* **2012**, *24*, 3445.
[20] D. Schliephake, A. Kauffmann, X. Cong, C. Gombola, M. Azim, B. Gorr, H. J. Christ, M. Heilmaier, *Intermetallics* **2019**, *104*, 133.
[21] S. Obert, A. Kauffmann, M. Heilmaier, *Acta Mater.* **2020**, *184*, 132.
[22] K. Beck, F. Hinrichs, C. Oskay, A. S. Ulrich, M. Heilmaier, M. C. Galetz, *Coatings* **2023**, *13*, 1712.
[23] M. Heilmaier, M. Krüger, H. Saage, J. Rösler, D. Mukherji, U. Glatzel, R. Völkl, R. Hüttner, G. Eggeler, C. Somsen, H. J. Christ, B. Gorr, S. Burk, *JOM* **2009**, *61*, 61.
[24] S. Obert, A. Kauffmann, R. Pretzler, D. Schliephake, F. Hinrichs, M. Heilmaier, *Metals* **2021**, *11*, 169.
[25] A. K. Misra, *J. Electrochem. Soc.* **1986**, *133*, 1029.
[26] B. S. Lutz, J. M. Alvarado-Orozco, L. Garcia-Fresnillo, G. H. Meier, *Oxid. Met.* **2017**, *88*, 599.
[27] M. Taylor, J. H. Perepezko, *Oxid. Met.* **2017**, *87*, 705.
[28] J. H. Perepezko, *Int. J. Refract. Met. Hard Mater.* **2018**, *71*, 246.
[29] E. Auchter, M. Taylor, J. H. Perepezko, *Oxid. Met.* **2020**, *93*, 387.
[30] K. Beck, T. König, A. Case, C. Oskay, M. C. Galetz, *Mater. Corros.* **2024**, *1*.
[31] S. S. Sunu, E. Prabhu, V. Jayaraman, K. I. Gnanasekar, T. Gnanasekaran, *Sens. Actuators B Chem.* **2003**, *94*, 189.
[32] R. Rathnasamy, V. Alagan, *Phys. E Low Dimens. Syst. Nanostruct.* **2018**, *102*, 146.
[33] M. G. Lawson, H. R. Kim, F. S. Pettit, J. R. Blachere, *J. Am. Ceram. Soc.* **1990**, *73*, 989.
[34] N. Horii, M. Kamide, A. Inouye, N. Kuzuu, *J. Ceram. Soc. Japan* **2010**, *118*, 318.
[35] T. P. S. Clair, J. M. Restad, S. T. Oyama, *J. Mater. Res.* **1998**, *13*, 1430.
[36] S. S. Sunu, E. Prabhu, V. Jayaraman, K. I. Gnanasekar, T. K. Seshagiri, T. Gnanasekaran, *Sens. Actuators B Chem.* **2004**, *101*, 161.
[37] C. R. S. V. Boas, J. M. Sturm, I. Milov, P. Phadke, F. Bijkerk, *Appl. Surf. Sci.* **2021**, *550*, 149384.
[38] R. F. de Farias, C. Airoldi, *J. Phys. Chem. Solids* **2003**, *64*, 2199.
[39] C. Gatzen, I. Smokovych, M. Scheffler, M. Krüger, *Adv. Eng. Mater.* **2021**, *23*, 2001016.
[40] A. Navrotsky, *Phys. Chem. Miner.* **1977**, *2*, 89.
[41] M. Lepple, K. Lilova, C. G. Levi, A. Navrotsky, *J. Mater. Res.* **2019**, *34*, 3343.
[42] A. Navrotsky, *J. Am. Ceram. Soc.* **2014**, *97*, 3349.
[43] F. Hoermann, *Z. für Anorg. Allg. Chem.* **1929**, *177*, 145.
[44] C. S. Giggins, F. S. Pettit, *Hot corrosion degradation of metals and alloys - A unified theory*, Pratt & Whitney Aircraft Group, East Hartford **1979**.
[45] R. A. Rapp, K. S. Goto, *ECS Proc. Vol.* **1981**, *1981*, 159.
[46] C. W. Bale, E. Bélisle, P. Chartrand, S. A. Decterov, G. Eriksson, A. E. Gheribi, K. Hack, I. H. Jung, Y. B. Kang, J. Melançon, A. D. Pelton, S. Petersen, C. Robelin, J. Sangster, P. Spencer, M. A. Van Ende, *Calphad* **2016**, *54*, 35.

[47] J. M. Hagan, *PhD thesis*, University of Virginia **2015**.
[48] B. E. Deal, A. S. Grove, *J. Appl. Phys.* **1965**, *36*, 3770.
[49] S. Obert, A. Kauffmann, S. Seils, S. Schellert, M. Weber, B. Gorr, H. J. Christ, M. Heilmaier, *J. Mater. Res. Technol.* **2020**, *9*, 8556.
[50] L. Wei, W. Shao, M. Li, C. Zhou, *Corros. Sci.* **2019**, *158*, 108099.
[51] P. Zhou, Y. Wang, Q. Liu, Y. Qiao, S. Chen, *Coatings* **2023**, *13*, 1031.
[52] H. Yu, Q. Fan, J. Li, D. Ma, J. Gong, C. Sun, *Corros. Sci.* **2023**, *212*, 110937.
[53] K. S. Goto, R. A. Rapp, *J. Electrochem. Soc.* **1978**, *125*, C371.
[54] R. A. Rapp, *Corros. Sci.* **2002**, *44*, 209.
[55] M. Dieterle, G. Mestl, *Phys. Chem. Chem. Phys.* **2002**, *4*, 822.

How to cite this article: K. Beck, T. König, E. Senvardarli, F. Hinrichs, M. Heilmaier, M. C. Galetz, *Mater. Corros.* **2024**, 1–10.
https://doi.org/10.1002/maco.202414491

APPENDIX A

See Figures A1 and A2.

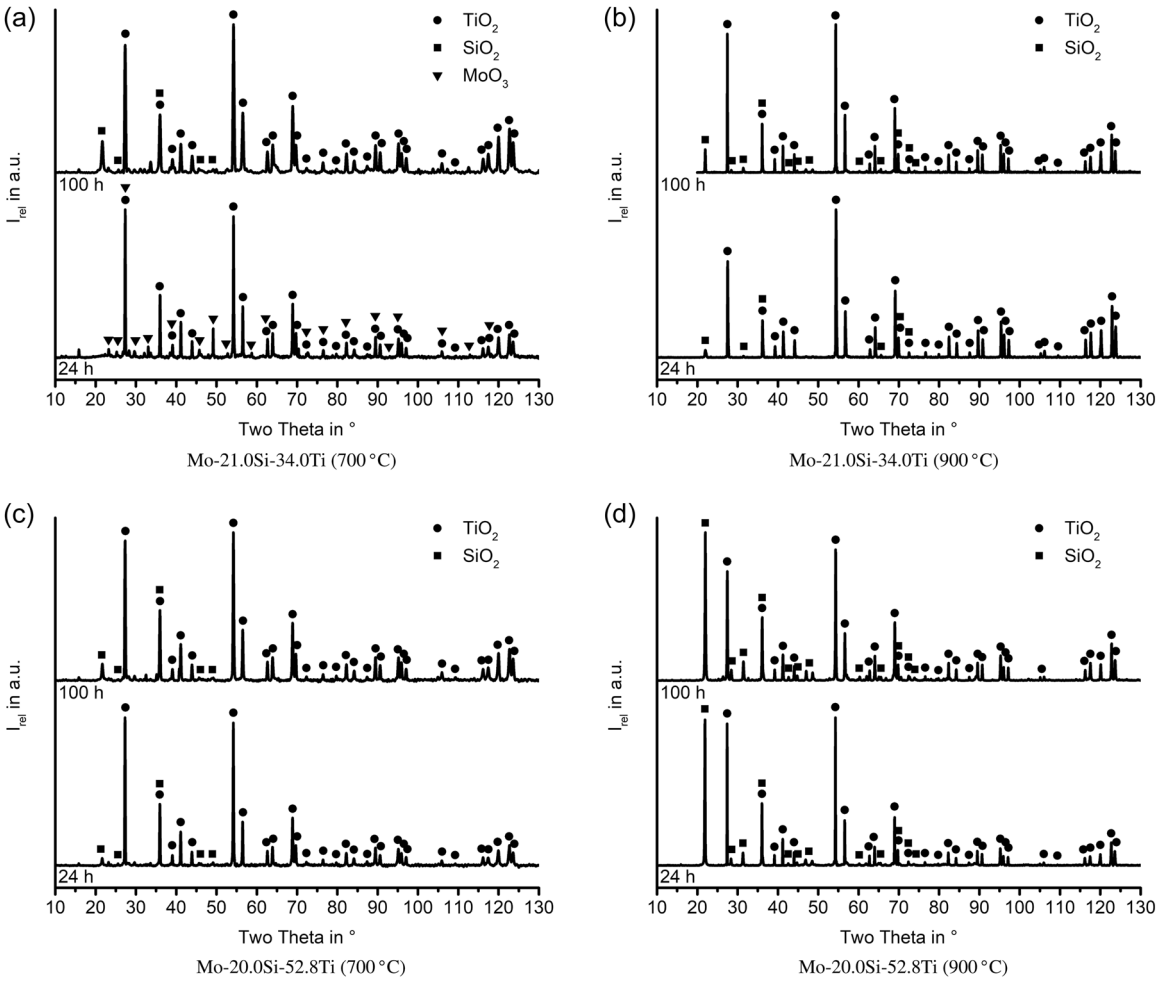

FIGURE A1 XRD diffractograms of the different oxides formed on the Mo-based alloys after hot corrosion at 700°C and 900°C in synthetic air + 0.1% SO_2 for 24 and 100 h.

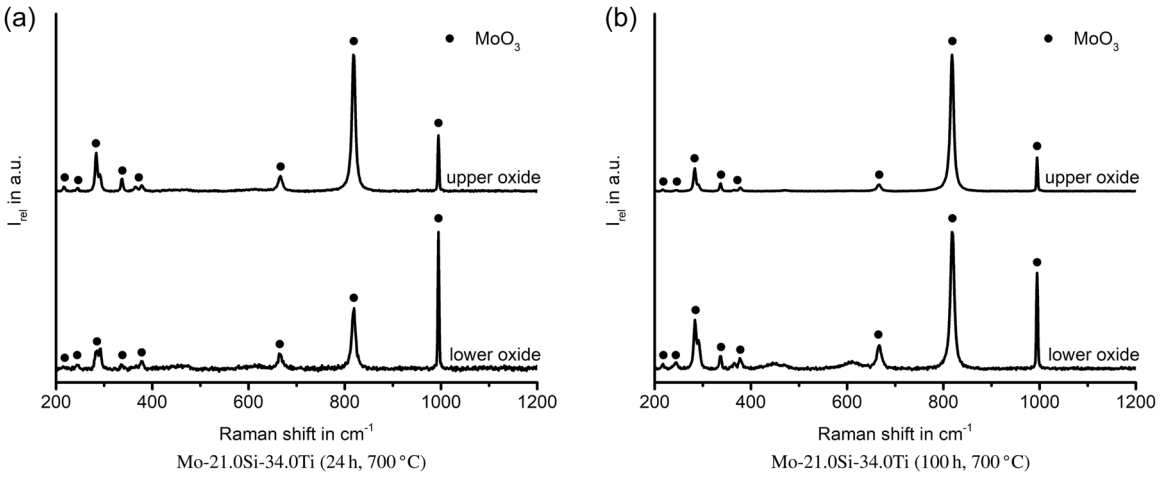

FIGURE A2 Normalized Raman spectra of the Mo oxides formed on the Mo–Si–Ti alloys after corrosion in synthetic air + 0.1% SO_2 for 24 and 100 h. Reference spectra from the literature were used to identify MoO_3.[55]